Theoretical and Applied Climatology
https://doi.org/10.1007/s00704-020-03111-9

ORIGINAL PAPER

A salient oceanic driver for the interannual variability of wintertime haze days over the Pearl River Delta region, China

Yue Chang[1] · Jing Wang[2] · Zhiwei Zhu[2] · Hua Deng[3] · Jinhai He[2] · Rui Lu[2]

Received: 7 November 2019 / Accepted: 20 January 2020

Abstract

This study explored the effect of sea surface temperature (SST) on the interannual variations in wintertime haze days (WHDs) in the Pearl River Delta (PRD) region (WHD_{PRD}) of China. Analyses unravel that SST anomalies in the adjoining area of the northern Indian and Pacific sector (the NIP region) can drive the interannual variations in the frequency of wintertime haze over the PRD region, which is deemed a salient oceanic driver. The SST anomalies have a stable and significant anticorrelation with the interannual component of the WHD_{PRD}. This anticorrelation is highest in the concurrent winter and thus exerts a strong influence on the variability of localized WHDs. Further observational and simulation results suggest that the cold SST anomalies in the NIP region can induce a large-scale east–west dipole pattern by triggering diabatic cooling to the northwest. This dipole resembles the pattern tied to a higher WHD_{PRD}, with an anticyclonic anomaly centered over the Indo-China Peninsula and a cyclonic anomaly centered over the western North Pacific. Under such circumstances, the PRD region is dominated by consistent northerly wind anomalies, facilitating the formation of two crucial processes responsible for a higher WHD_{PRD}: the northward transportation of aerosols and a decrease in local wet deposition.

1 Introduction

The Pearl River Delta (PRD) region (Fig. 1) in southern China has both a modern manufacturing industry and a high urban population (Tong et al. 2018). Accelerated industrialization and urbanization in recent years (Wu et al. 2013) have led to an increase in haze events (Wu et al. 2007; Cheng et al. 2019; Mao et al. 2019; Zhang et al. 2019). These haze events have deleterious effects on human health (Tie et al. 2009; Wu et al. 2019), vehicular traffic (Wu et al. 2005), and agricultural productivity (Tie et al. 2016). As a consequence, the Chinese government has launched a number of initiatives to mitigate air pollution in this region (Jiang et al. 2015; Zheng et al. 2017).

Haze events in eastern China mainly occur in the boreal winter (Ding and Liu 2014; Mao et al. 2019) and many studies have explored the causes of the variability in wintertime haze. It has been found that, in addition to anthropogenic aerosol emissions, anomalies in climatic factors—such as the East Asian winter monsoon (EAWM) (e.g., Cheng et al. 2016; Li et al. 2016; Yang et al. 2016), the sea surface temperature (SST) (e.g., Xiao et al. 2015; You et al. 2018; Feng et al. 2019), and cryospheric forcing (e.g., Wang et al. 2015; Zou et al. 2017; Yin et al. 2019)—also affect the variability of haze events. When specifically focusing on the variability of haze events in southern China, previous studies have found that wet deposition related to precipitation and the transportation of local and nonlocal atmospheric aerosols are the two crucial factors responsible for the variability in the frequency of the local wintertime haze days (WHDs) (Wang et al. 2017; Li et al. 2018; He et al. 2019). On interannual timescale, the El Niño–Southern Oscillation (ENSO) remotely influences the variability in WHDs in southern China via the modulation of

Yue Chang and Jing Wang contributed equally to this work.

✉ Zhiwei Zhu
zwz@nuist.edu.cn

[1] Guangdong Meteorological Service, Guangzhou, China

[2] Key Laboratory of Meteorological Disaster, Ministry of Education (KLME)/Joint International Research Laboratory of Climate and Environment Change (ILCEC)/Collaborative Innovation Center on Forecast and Evaluation of Meteorological Disasters (CIC-FEMD), Nanjing University of Information Science and Technology, Nanjing, China

[3] China Meteorological Administration, Institute of Tropical and Marine Meteorology, Guangzhou, China

Published online: 05 February 2020

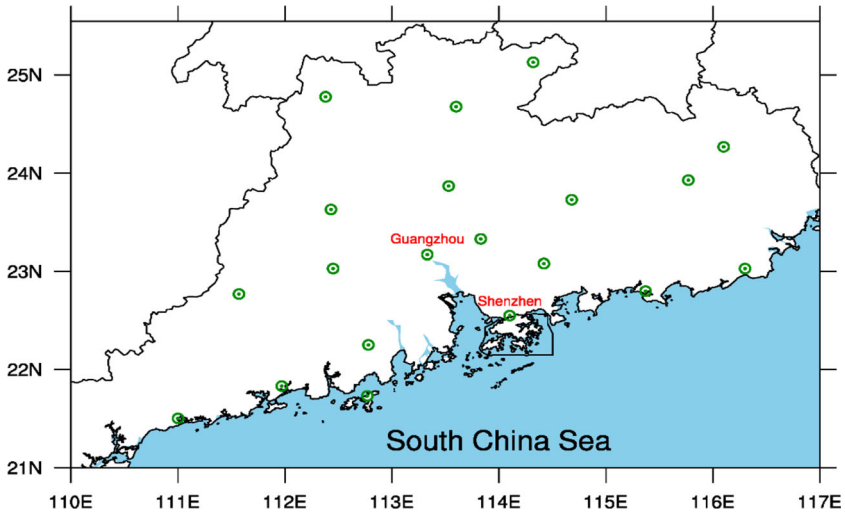

Fig. 1 Location of the 20 meteorological stations in the PRD region

these two factors; more specifically, the cold (warm) phase of the ENSO leads to a higher (lower) number of WHDs in southern China (Gao and Li 2015; Li et al. 2017; Zhao et al. 2018; Cheng et al. 2019; He et al. 2019).

Our analysis found a novel oceanic driver for the interannual variation in WHDs in the PRD region (WHD_{PRD}). This paper introduces this driver and explores the underlying physical mechanisms. The PRD region is one of the major haze-polluted regions of China (Leung et al. 2018; Mao et al. 2019; Zhang et al. 2019) and this work provides scientific support for central and local governments to prevent and mitigate wintertime haze pollution events. The rest of this paper is structured as follows. Section 2 describes the datasets and methods. Section 3 presents the related circulation and SST patterns and the underlying mechanisms. Section 4 gives our further discussion. Conclusions are provided in the final section.

2 Data and methodology

2.1 Data

We used the following five datasets in this study: (1) ground-timing observations at 02:00, 08:00, 14:00, and 20:00 (Beijing local time) provided by the National Meteorological Information Center of China (http://data.cma.cn/); (2) monthly mean atmospheric data with a horizontal resolution of 2.5° and total cloud cover (with the entire atmosphere considered as a single layer; 192 points × 94 points in the horizontal direction) from the National Centers for Environmental Prediction–National Center for Atmospheric Research (NCEP/NCAR) Reanalysis I dataset (Kalnay et al. 1996); (3) global monthly mean SST data obtained from the National Oceanic and Atmospheric Administration Extended Reconstructed SST version 5 dataset (ERSST v5; Huang et al. 2017) at a horizontal resolution of 2°; (4) the monthly anomaly precipitation (2.5° × 2.5°) from the precipitation reconstruction dataset of the National Oceanic and Atmospheric Administration (PREC; Chen et al. 2002) and monthly mean precipitation (2.5° × 2.5°) data from the Global Precipitation Climatology Project (Adler et al. 2003); and (5) the monthly mean planetary boundary layer height (PBLH) taken from the European Centre for Medium-Range Weather Forecasts Interim (ERA-Interim) reanalysis dataset on a 1° × 1° global grid (Dee et al. 2011). The temporal coverage of these datasets was from 1980 to 2016.

2.2 Methodology

Our definition of a haze day was consistent with previous studies (e.g., Chen and Wang 2015; Yang et al. 2016) and was based on the ground-timing observations of relative humidity, visibility, and wind speed. Using the method of Wang et al. (2018), the mean number of haze days ($\overline{\mathrm{NHD}}$) in the PRD was calculated by:

$$\overline{\mathrm{NHD}} = \frac{1}{n}\sum_{i=1}^{n} N \tag{1}$$

where n is the number of observational sites located within the PRD region ($n = 20$ here) (Fig. 1) and N is the number of haze days at a site for each winter.

We extracted the interannual component of WHD_{PRD} by removing the interdecadal constituent of the detrended original time series of WHD_{PRD}. The 9-year running mean method was used to obtain the corresponding interdecadal component. Because the first 4 years and the last 4 years of the interdecadal component of the WHD_{PRD} are unavailable, an estimate algorithm was used to resolve the problem of missing years caused by tapering when computing the running mean (Zhu and Li 2017; Wang et al. 2019). For example, the interdecadal component of the WHD_{PRD} for 2015 and 2016 could be obtained by the mean of 2011–2016 and 2012–2016, respectively.

Figure 2 shows that the temporal evolution of the interannual component of the WHD_{PRD} has remarkable year-to-year variations.

Correlation and linear regression analyses were used to identify the atmospheric circulation patterns and SST anomalies (SSTAs) associated with the interannual changes in the WHD_{PRD}. A two-tailed Student's *t* test was applied to evaluate the statistical significance of the analyses. The boreal summer, autumn, and winter were defined as the seasonal mean for June–August (JJA), September–November (SON), and December–February (DJF), respectively.

2.3 Model

We used a linear anomaly atmospheric general circulation model developed from the Geophysical Fluid Dynamics Laboratory global spectrum dry numerical model (Held and Suarez 1994). The horizontal resolution was T42 with five sigma (σ) levels in the vertical direction [$\sigma = p/ps$, where p is the pressure and ps is the surface pressure; interval, 0.2; top level, $\sigma = 0$; bottom level, $\sigma = 1$]. A realistic winter mean state, obtained from the long-term mean of the NCEP/NCAR reanalysis data, was prescribed as the model basic state. This model has been widely used to examine the teleconnection triggered downstream by specific atmospheric cooling/warming processes (e.g., Zhu and Li 2016, 2018).

3 Results

3.1 Circulation patterns tied to the interannual variability of the WHD_{PRD}

Before delving into the oceanic driver, we revisited the winter climatic background and examined both the large-scale and localized circulation anomalies associated with the interannual change in WHD_{PRD}. Following the way of previous studies (e.g., Zhao et al. 2018; He et al. 2019), we focused on the circulations in the lower and middle troposphere, which could exert more notable impacts on the haze variability. Figure 3 shows the climatological mean 500 hPa geopotential height (Z500), 850 hPa winds (UV850), total cloud cover, and precipitation. A noticeable mid-tropospheric trough, which is one of the main components of the EAWM circulation system, is located over the coastal areas of East Asia (Fig. 3). Behind this trough, the mid-latitudes of eastern China (east of 110° E) are controlled by northwesterly winds, concomitant with decreased rainfall (Fig. 3). In stark contrast, the low-latitude PRD region is dominated by southerly winds (Fig. 3), showing its insignificant relation with the EAWM. As such, climatologically, the PRD region has more precipitation (Fig. 3) than northern China, which could reduce the occurrence of wintertime haze via wet deposition (Li et al. 2017). It is therefore plausible to suggest that the frequency of the WHD_{PRD} could be increased if the rainy conditions are interrupted. One may ask whether a higher WHD_{PRD} is related to the interference of such rainy conditions. To answer this question, we examined the atmospheric circulation patterns associated with the year-to-year changes in the WHD_{PRD}.

Figures 4 and 5 show the anomalous large-scale and localized circulation patterns regressed on the interannual WHD_{PRD} time series. As suggested, the circulation patterns tied to a higher WHD_{PRD} are distinct from those in the climatological state. Figure 4 a shows that the mid-tropospheric northerly wind anomalies favor a higher WHD_{PRD}. The PRD region is dominated by anomalous northerly winds in the lower atmosphere (Figs. 4b and 5d). Further analysis suggested that a large-scale dipole pattern with an anomalous anticyclone (high pressure) centered over the Indo-China Peninsula and a cyclone (low pressure) centered over the western North Pacific (WNP) (Fig. 4a) is responsible for these mid-tropospheric northerly winds. Note that a significant low-level cyclonic anomaly with two centers can also be seen over the WNP with a quasi-barotropic structure (Fig.4b). Although the anticyclonic anomaly over the Indo-China Peninsula is not clearly seen in the lower troposphere as a result of the influence of the Tibetan Plateau, we can observe anticyclonic wind shear over this region (Fig. 4b), which also contributes to the formation of lower-level northerly wind anomalies in conjunction with the marked cyclonic anomaly.

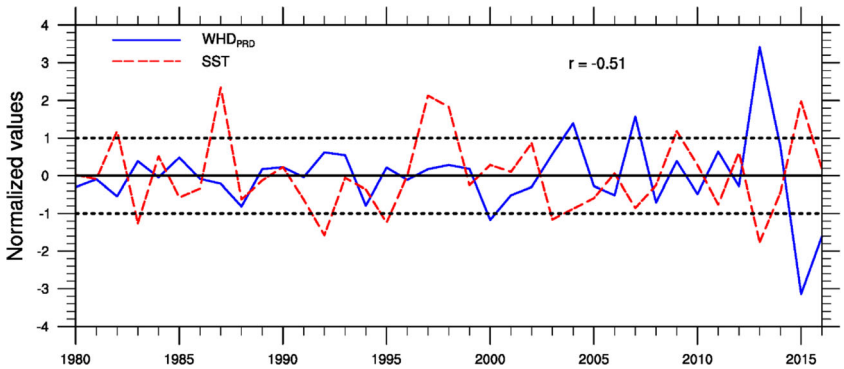

Fig. 2 Normalized time series of the interannual component of the WHD_{PRD} (blue line) and the simultaneous detrended SST in the NIP region (red line) for the period 1980–2016. The temporal correlation coefficient (*r*) between them is labeled. The horizontal dashed lines denote ± 1 standard deviation

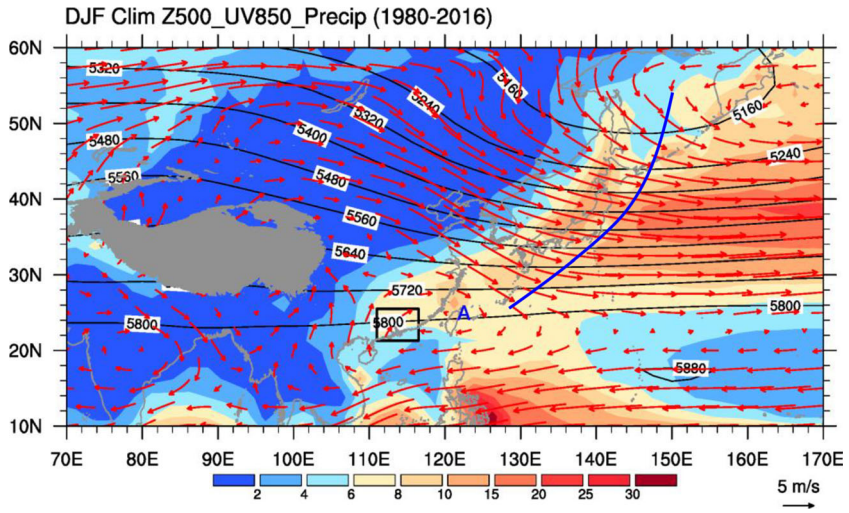

Fig. 3 The climatological mean (1980–2016) boreal winter Z500 (contours; gpm), UV850 (vectors; m s^{-1}) and precipitation (shaded; mm day^{-1}). The blue solid line depicts the mid-tropospheric trough. The gray shaded area denotes the Tibetan Plateau and the black frame delineates the research domain of the PRD region (21.3–25.5° N, 111.0–116.5° E). The letter A represents the center of anticyclonic circulation. The precipitation data are from the Global Precipitation Climatology Project reconstruction dataset

Under these circumstances, the PRD region is dominated by consistent downward anomalies in motion (Fig. 4), inducing a localized significant decrease in the total cloud cover (Fig. 5c) and precipitation (Fig. 5b), together with a resultant decrease in the relative humidity at the surface (Fig. 5a). As such, wet deposition is repressed in this region. The near-surface northerly winds (Fig. 5d) with positive wind speed anomalies to the north of the PRD region (Fig. 5e) facilitate the long-range transport of large amounts of airborne pollutants from northern China to the PRD region through cold surges (Wang et al. 2017). These advected pollutants accumulate within the boundary layer of the PRD region with the help of the local near-surface positive vorticity (Fig. 5f). However, sunny conditions prevail in the PRD region as a result of the suppressed precipitation/cloud cover, which hampers the formation of stable atmospheric stratification at lower levels (Fig. 5g) and increases the PBLH (Fig. 5h) by heating of the land surface under anomalous sunny conditions. As a consequence, a higher WHD_{PRD} corresponds to a local increase in the PBLH and insignificant low-level atmospheric stratification, in agreement with the results of He et al. (2019).

3.2 Searching for the driver(s) of the interannual variability in the WHD_{PRD}

To search for the significant oceanic driver(s) that exerts a stable influence on the variability of haze on an interannual timescale, we examined the relationship between the interannual component of the WHD_{PRD} and the large-scale SSTAs in the preceding summer (Fig. 6a) and autumn (Fig. 6b) and in the concurrent winter (Fig. 6c). The most stable area with a long-lasting significant negative correlation passing the 95% confidence level is in the adjoining area of the northern Indian and Pacific (NIP) sector around (8–22° N, 80–122° E). The

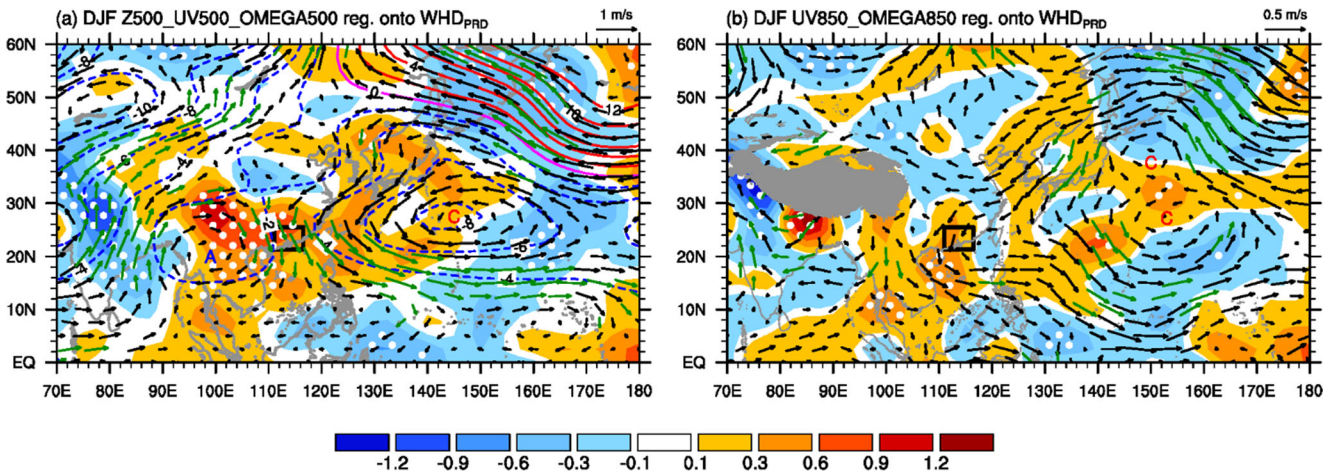

Fig. 4 Regression maps of the boreal winter (**a**) 500 hPa omega (shaded; 10^{-2} Pa s^{-1}), 500 hPa winds (UV500; vectors; m s^{-1}), and Z500 (contours; gpm) and (**b**) 850 hPa omega (shaded; 10^{-2} Pa s^{-1}) and UV850 (vectors; m s^{-1}) onto the normalized interannual component of the WHD_{PRD}. Regression coefficients that are significant at the 90% confidence level are stippled. The wind vectors with statistical significance above the 90% confidence level are colored in green. The gray shaded area denotes the Tibetan Plateau and the black frame delineates the research domain of the PRD region. The letters A and C represent the centers of anticyclonic and cyclonic anomalies, respectively

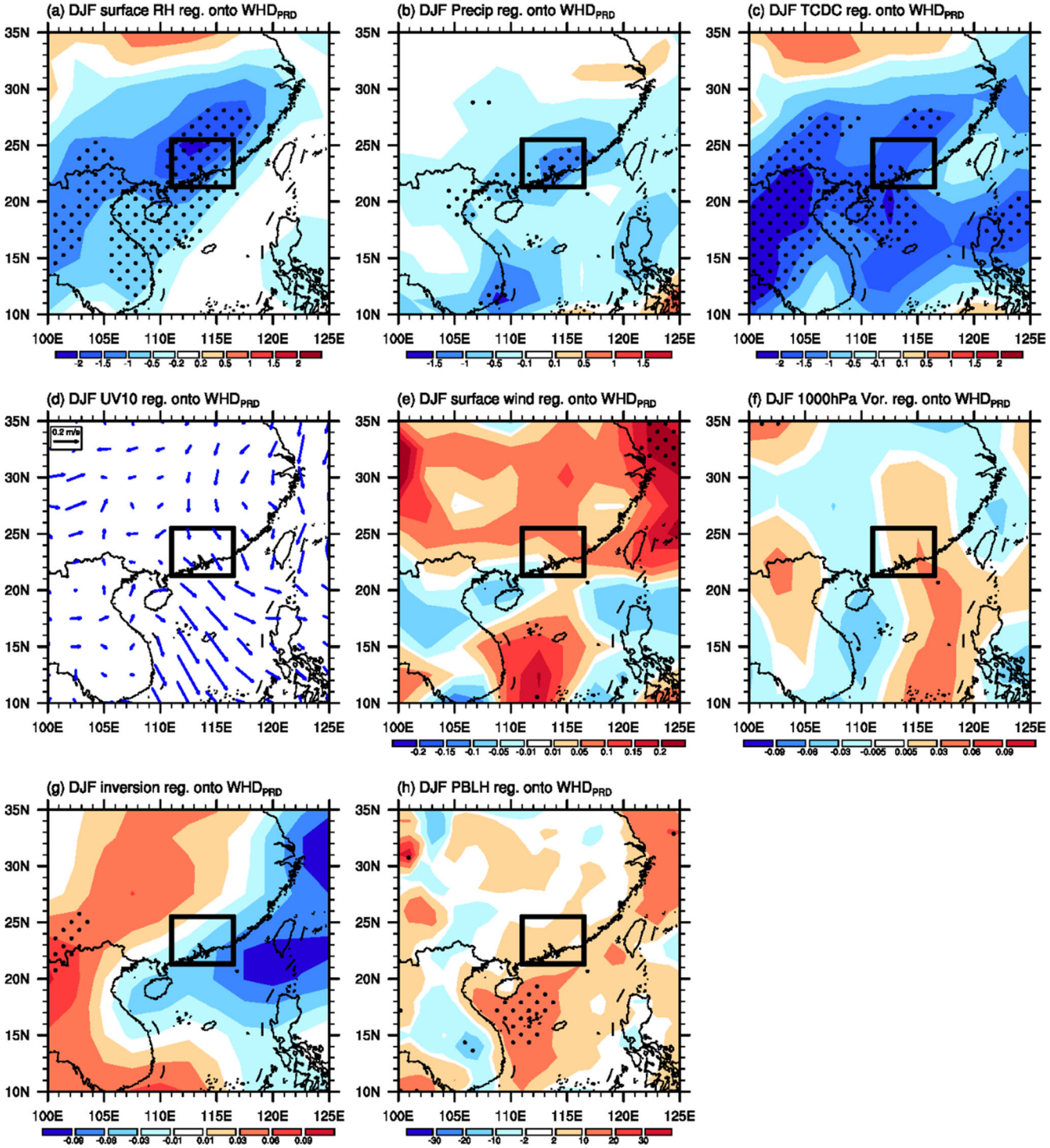

Fig. 5 Regressed patterns of the boreal winter meteorological parameters onto the interannual component of the WHD_{PRD}, including the surface relative humidity (shaded; %) (**a**), precipitation (shaded; mm day^{-1}) (**b**), total cloud cover (shaded; %) (**c**), surface winds (vectors; m s^{-1}) (**d**), surface wind speed (shaded; m s^{-1}) (**e**), 1000 hPa relative vorticity (shaded; 10^{-5} s^{-1}) (**f**), air temperature between 850 and 1000 hPa (shaded; °C) (**g**), and the PBLH (shaded; m) (**h**). Regression coefficients significant at the 90% confidence level are stippled. The black frame outlines the research domain of the PRD region. The precipitation data are from the PREC reconstruction dataset

temporal correlation coefficient between the interannual component of the WHD_{PRD} and the concurrent detrended SST in the NIP region is − 0.51 (Fig. 2), exceeding the 99% confidence level. The SSTAs in the NIP region capture the extreme values of the WHD_{PRD} well (e.g., the highest WHD_{PRD} in 2013 and the lowest in 2015). It is interesting to note that, the haze frequency is not significantly correlated with equatorial eastern Pacific SST (Fig. 6). The temporal correlation

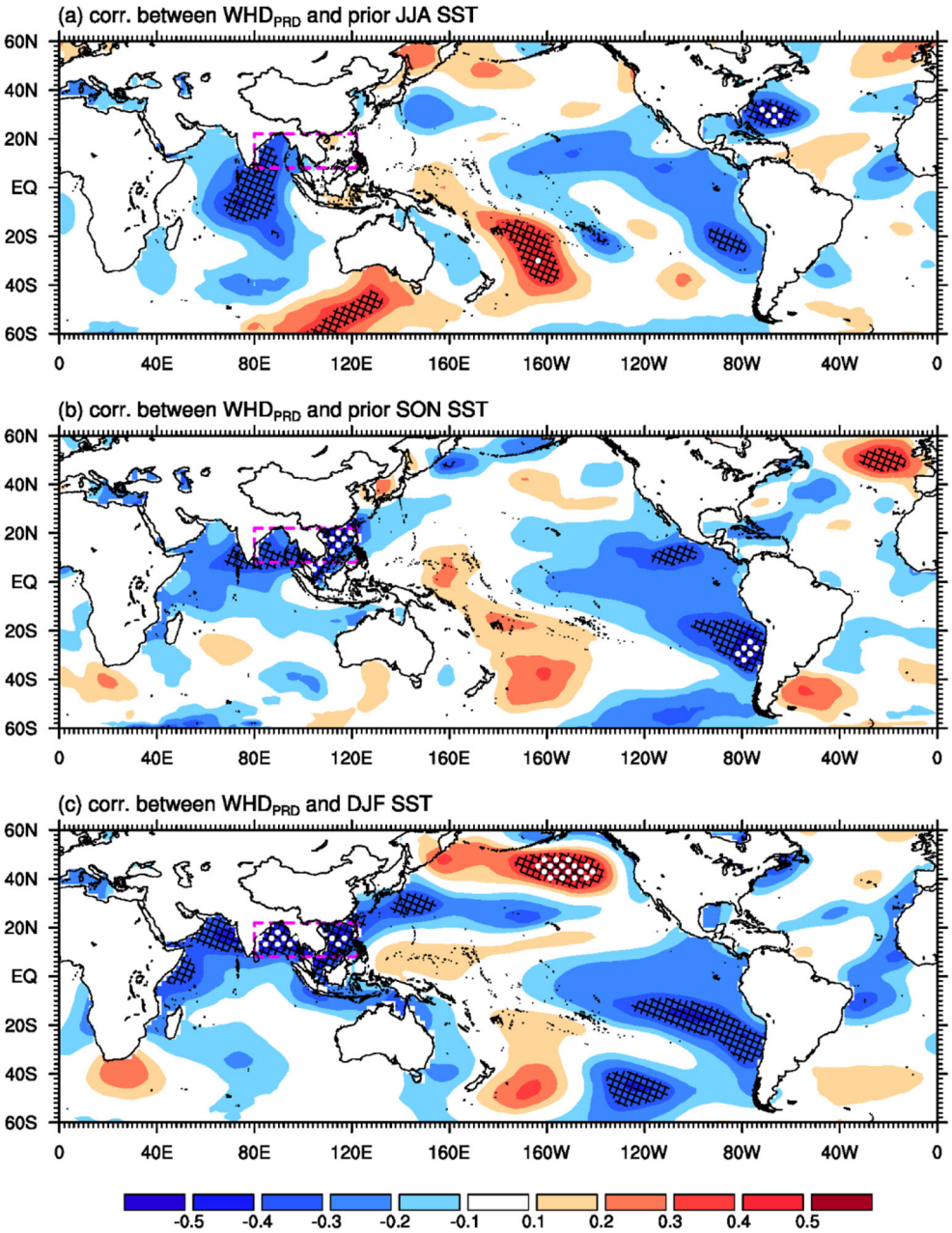

Fig. 6 Correlation coefficients between the interannual component of the WHD_{PRD} and SSTA in the region (60° S–60° N) during JJA (**a**), SON (**b**), and DJF (**c**). Correlation coefficients significant at the 99% (95%) confidence level are stippled (cross-hatched). The magenta dashed box (8–22° N; 80–122° E) denotes the key area with significant correlations

coefficient between the number of WHD_{PRD} and the Niño-3.4 index is only − 0.23 and does not exceed the 90% confidence level. As a result of the stable and significant relationship between the frequency of WHD_{PRD} and the SSTAs in the NIP region, SSTAs in the NIP region can be regarded regard as the salient oceanic driver for the interannual variability in WHD_{PRD} rather than the ENSO.

3.3 Physical mechanisms

Next, we investigate the physical mechanisms by which the SSTAs in the NIP region affect the interannual changes in the frequency of wintertime haze in the PRD region. Because the corresponding maximum anticorrelation occurs in the simultaneous winter (Fig. 6c), we conducted regression and composite analyses associated with the DJF SSTAs in the NIP region. For convenience, we constructed a NIP index (NIPI) by averaging the SSTAs in the NIP region during DJF and multiplied this by − 1 to express the influence of negative SSTAs in the NIP region. A positive NIPI therefore corresponds to increased WHD_{PRD}.

To illuminate the associated physical mechanisms, we first performed regression analyses on the detrended NIPI. Figs. 7 and 8 show that, overall, the spatial patterns of circulation (i.e., the dipole pattern) and the lower boundary conditions regressed against the NIPI resemble those tied to the interannual variation in the WHD_{PRD} (Figs. 4 and 5). A quasi-barotropic cyclonic

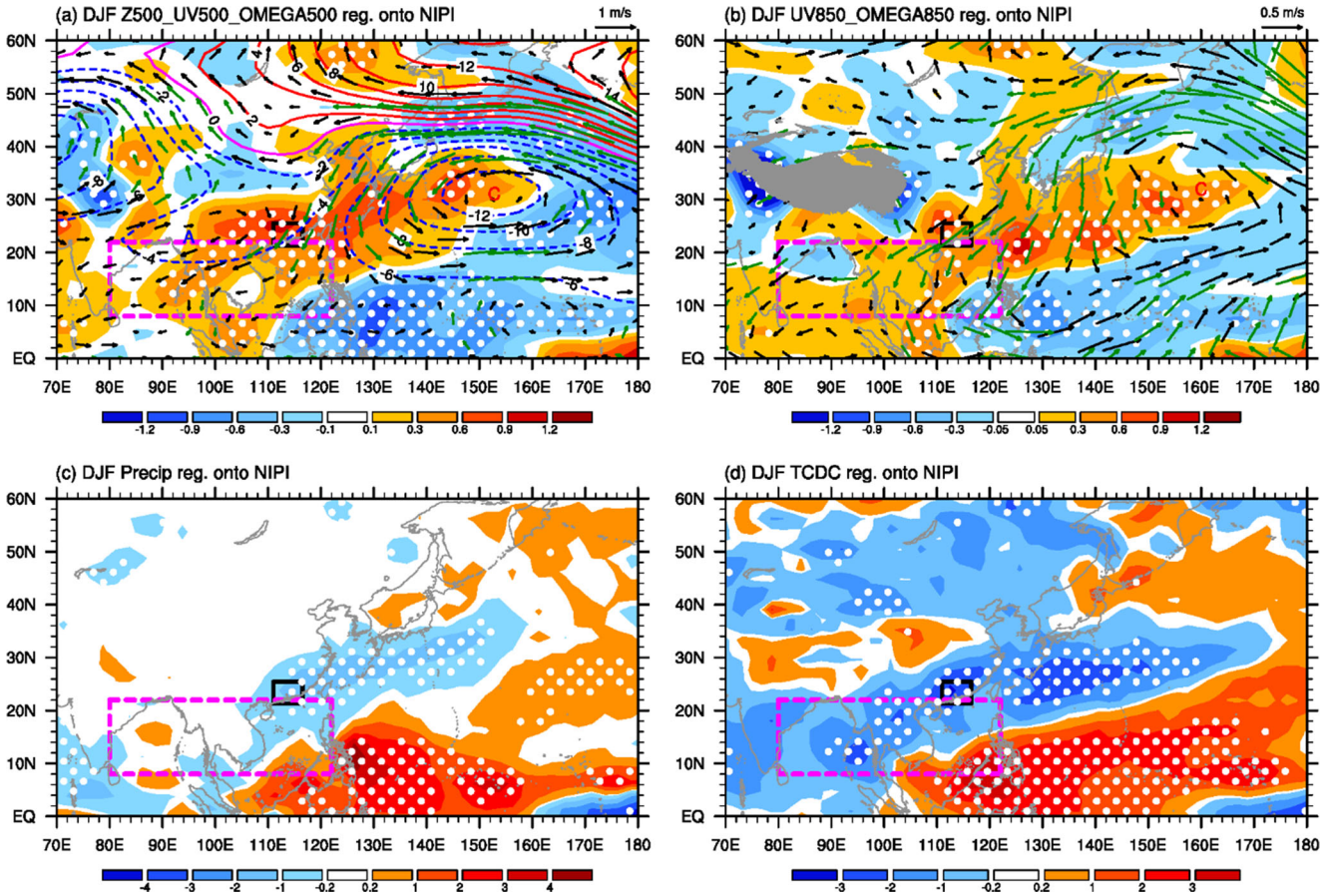

Fig. 7 Regression maps of the boreal winter (**a**) 500 hPa omega (shaded; 10^{-2} Pa s^{-1}), UV500 (vectors; m s^{-1}), and Z500 (contours; gpm), (**b**) 850 hPa omega (shaded; 10^{-2} Pa s^{-1}) and UV850 (vectors; m s^{-1}), (**c**) precipitation (shaded; mm day^{-1}), and (**d**) total cloud cover (shaded; %) onto the normalized detrended NIPI. Regression coefficients that are significant at the 90% confidence level are stippled. The wind vectors with statistical significance above the 90% confidence level are colored in green. The gray shaded area denotes the Tibetan Plateau and the black frame delineates the research domain of the PRD region. The letters A and C represent the centers of anticyclonic and cyclonic anomalies, respectively. The precipitation data are from the PREC reconstruction dataset. The magenta dashed box (8–22° N; 80–122° E) denotes the key area with significant correlations

anomaly appears over the WNP in association with the cold SSTA in the NIP region. In addition, the mid-tropospheric anticyclonic anomaly and low-level anticyclonic wind shear emerge over the Indo-China Peninsula (Fig. 7a, b). Conspicuously, the PRD region is affected by a zonal geopotential dipole pattern similar to that tied to a higher WHD_{PRD}, with consistent northerly anomalies and an increase in downward motion anomalies (Figs. 7a, b and 8b), inhibiting the local convective activity. Therefore, the PRD region and its surroundings are controlled by the suppressed precipitation (Fig. 7c) and cloud cover (Fig. 7d) and the resultant significantly decreased surface relative humidity (Fig. 8a). Localized sunny conditions are enhanced in such a scenario, facilitating dampening of the low-level stability (Fig. 8e) and increasing the PBLH (Fig. 8f). In addition, although the convergence tends to be weaker (Fig. 8d) than that tied to a higher WHD_{PRD} (Fig. 5f), the positive northerly anomalies (Fig. 8b, c) still favor an increase in the frequency of local haze through the northward transport of pollutants toward the PRD region.

This anticyclonic anomaly and the concomitant suppressed precipitation/cloud cover (diabatic cooling) over the PRD and its surroundings (Fig. 7) are connected to the Gill–Matsuno-type response (Matsuno 1966; Gill 1980) to the cold SSTAs in the NIP region. To the east of the cold SSTAs, westerly wind anomalies are excited as a Gill-type Kelvin wave response (Yu et al. 2016), which further induces a remote cyclonic anomaly over the WNP by reinforcing the adjacent cyclonic vorticity. To validate this proposed physical process, we performed an experiment to simulate the response to the cooling induced by negative SSTAs in the NIP region (C_NIP; Fig. 9). C_NIP was imposed with specified cooling centered over the region to the northwest of NIP (centered at 23.72° N, 101.25° E), where the regressed precipitation/cloud cover was the most significant (Fig. 7). The cooling had a cosine-squared profile in an elliptical region in the horizontal direction. To avoid undue influence of topography of the Tibetan Plateau, the maximum diabatic cooling rate was set at $\sigma = 0.5$ (~ 500 hPa), with an amplitude of 1 K day^{-1}. Figure 9 shows

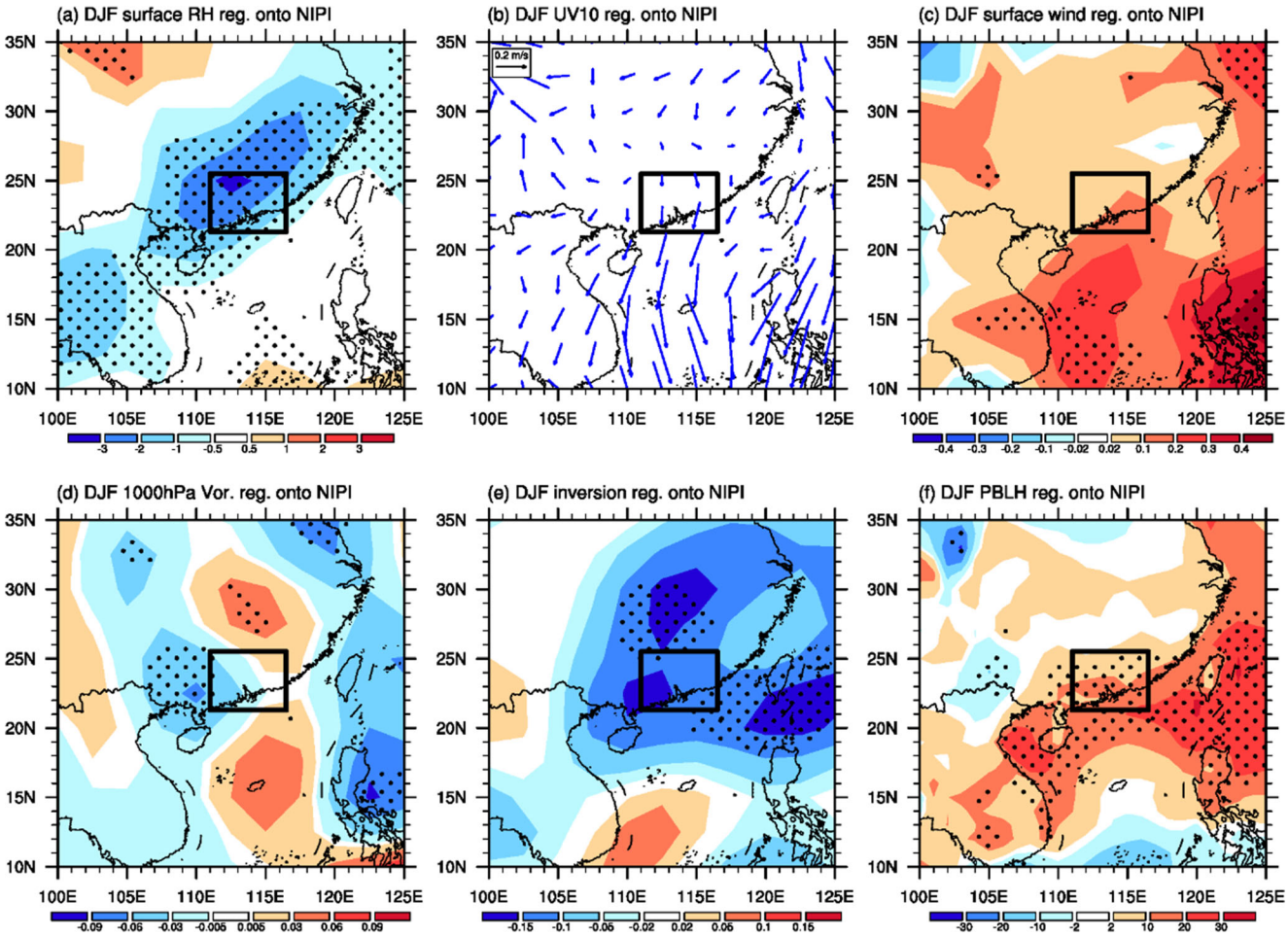

Fig. 8 Regressed patterns of the boreal winter meteorological parameters onto the normalized detrended NIPI, including surface relative humidity (shaded; %) (**a**), surface winds (vectors; m s^{-1}) (**b**), surface wind speed (shaded; m s^{-1}) (**c**), 1000 hPa relative vorticity (shaded; 10^{-5} s^{-1}) (**d**), air temperature between 850 and 1000 hPa (shaded; °C) (**e**), and PBLH (shaded; m) (**f**). Regression coefficients that are significant at the 90% confidence level are stippled. The black frame outlines the research domain of the PRD region

the time evolution of the response of the anomalous Z500 and UV500 in C_NIP. A wave-type structure with an equilibrium state can be clearly seen from days 15 to 60. The anticyclonic anomaly to the northwest of the NIP region was first formed around day 5 and then a remote cyclonic anomaly over the WNP was gradually excited via the generation of the westerly anomalies. After day 15, a stable zonal geopotential height dipole pattern that resembled the pattern shown in Fig. 7a was established, inducing more enhanced northerly wind anomalies over the PRD region. The corresponding lower-level (700 hPa) anticyclonic anomaly is unclear due to the topography of the Tibetan Plateau, but the remote low-level cyclonic anomaly counterpart was still triggered (Fig. 10).

4 Discussion

The simultaneous northerly wind anomalies are conducive to a higher WHD_{PRD} (Figs. 4 and 5d). One may wonder whether this above-normal WHD_{PRD} was closely associated with the strengthened EAWM. Following the method of Li et al. (2016), we examined the relationships between the WHD_{PRD} and three different types of EAWM index (EAWMI), including the EAWMI reflecting the near-surface meridional winds (Ji et al. 1997; $EAWMI_{Ji}$), the East Asian Trough (Wang and He 2012; $EAWMI_{Wang}$), and the subtropical upper level westerly jet (Jhun and Lee 2004; $EAWMI_{Jhun}$). The $EAWMI_{Ji}$ and $EAWMI_{Wang}$ were multiplied by − 1, so that a high index corresponds to a strong EAWM. Figure 11 shows that these indices hardly capture the higher or lower values of WHD_{PRD}, and none of the extreme values. The temporal correlation coefficients between the inter-annual WHD_{PRD} and the detrended $EAWMI_{Ji}$ ($EAWMI_{Wang}$; $EAWMI_{Jhun}$) are only 0.21 (0.24; − 0.07), all of which are insignificant at the 90% confidence level. Thus, the EAWM is not significantly tied to the interannual variability in the WHD_{PRD}. In effect, according to Luo and Wang (2017), the PRD region is not located in the "heart" region of the EAWM. Therefore, the EAWM may exert a less profound effect on the frequency of

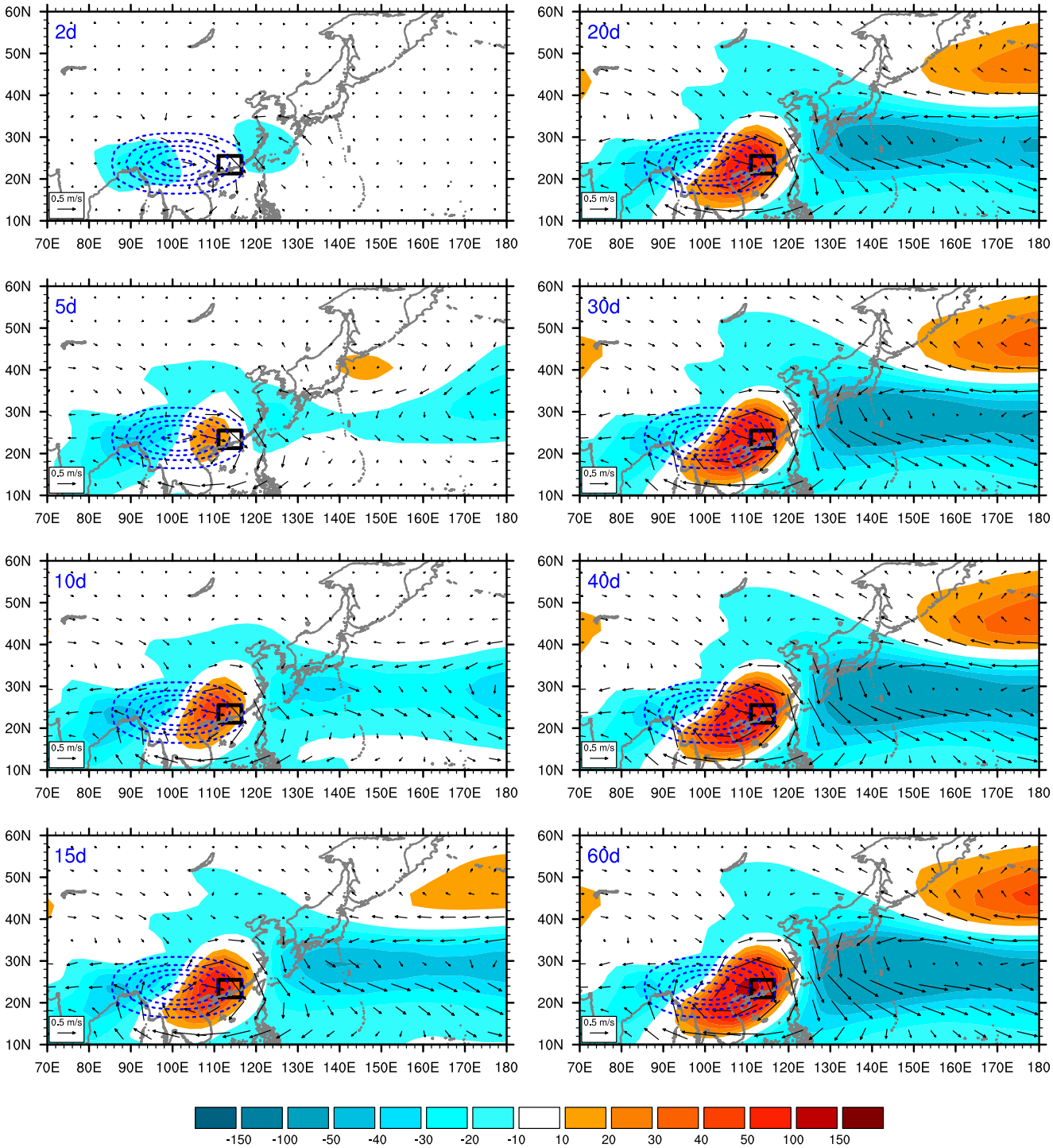

Fig. 9 Temporal evolution (from days 2 to 60) of the response of anomalous Z500 (shaded; 10 gpm) and UV500 (vectors; m s^{-1}) in C_NIP. The blue dashed contours indicate the imposed idealized cooling. The black frame delineates the research domain of the PRD region

haze in this region. Furthermore, the atmospheric conditions tied to the variability of haze in North China are very different. The decreased surface winds over North China, together with warmer and moister air, are responsible for the increase in the frequency of in situ winter/autumn haze. The northeast Asian anticyclonic anomaly is the key system affecting these conditions through the resultant low-level southerly wind anomalies on its western flank (e.g., Wang et al. 2018, 2019; Yin et al. 2019).

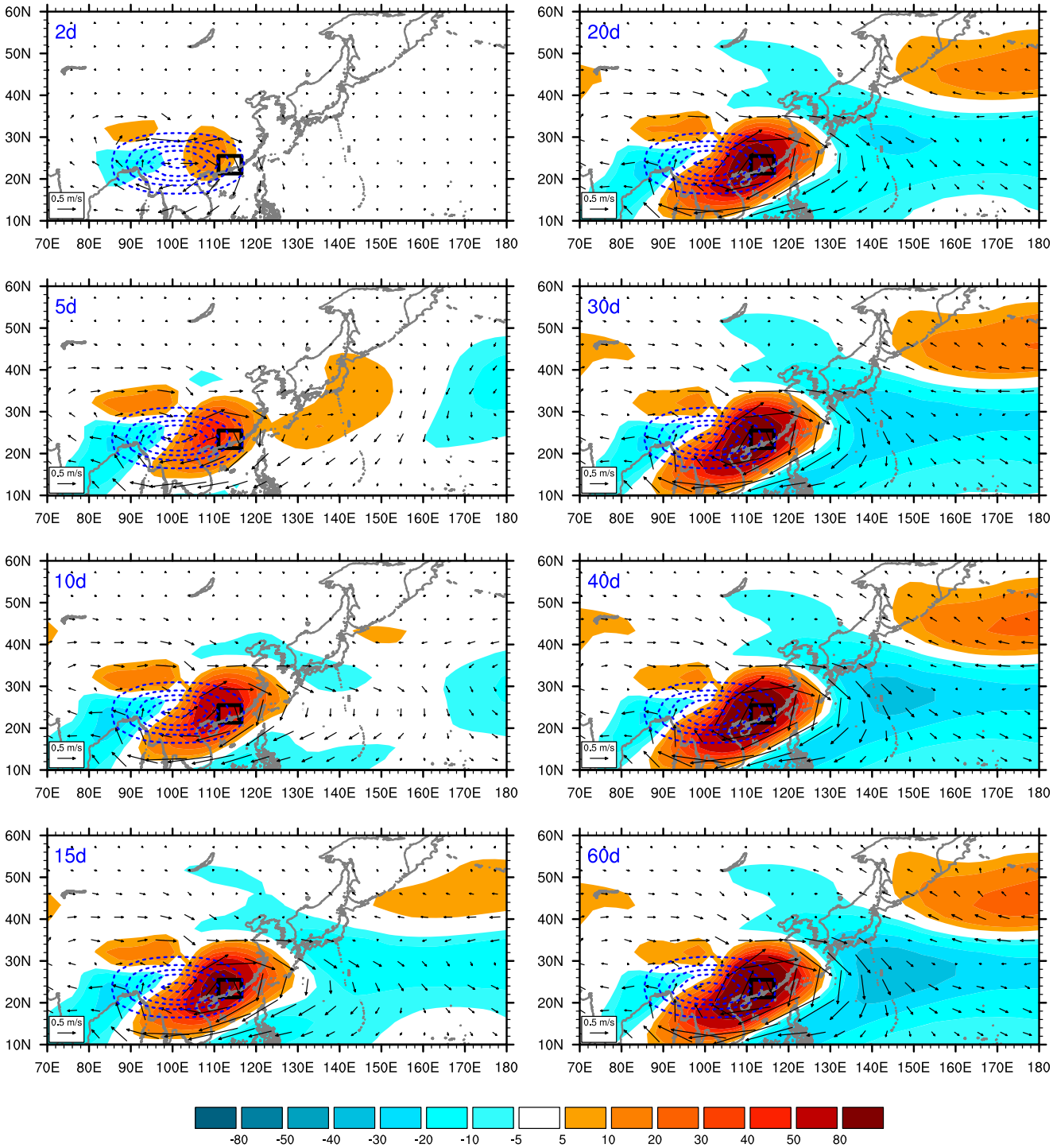

Fig. 10 Temporal evolution (from days 2 to 60) of the response of anomalous 700 hPa geopotential height (shaded; 10 gpm) and 700 hPa winds (vectors; m s^{-1}) in C_NIP. The blue dashed contours indicate the imposed idealized cooling. The black frame delineates the research domain of the PRD region

5 Conclusions

The interannual variations in the WHD_{PRD} and its relationship with the circulation anomalies and SSTAs for the period 1980–2016 were investigated. We found that the number of WHD_{PRD} has a significantly negative correlation with the SSTAs in the NIP region, which may act as a salient driver of the frequency of wintertime haze in the PRD region. This out-of-phase relationship is highest in the winter and has a profound impact on the variability of haze in DJF. We derived an index associated with the DJF SST in the NIP region (NIPI) and this was significantly correlated with the concurrent WHD_{PRD} at the 99% confidence level.

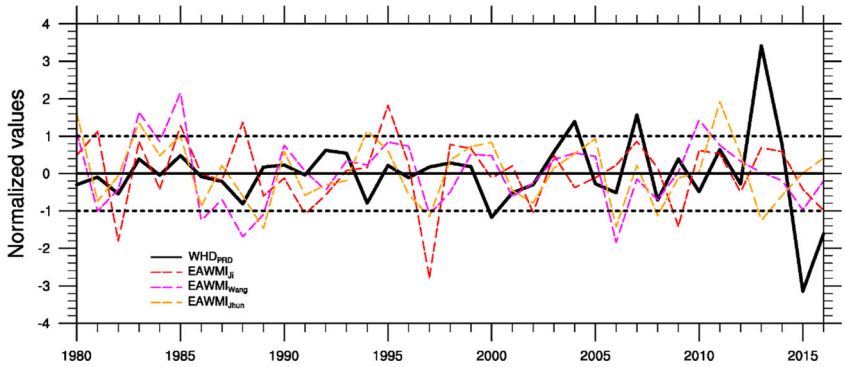

Fig. 11 Time series of the normalized interannual component of the WHD_{PRD} (black), along with three detrended EAWM indices [$EAWMI_{Ji}$ (red), $EAWMI_{Wang}$ (magenta), and $EAWMI_{Jhun}$ (yellow)] for the period 1980–2016

We propose a physical mechanism to explain how the cooling of the SSTs in the NIP region influences the interannual variability in the WHD_{PRD}. The cold SSTAs induce a large-scale east–west dipole pattern by triggering diabatic cooling to the northwest, with one anticyclone lobe centered over the Indo-China Peninsula and a quasi-barotropic cyclonic cell centered over the WNP. As a result of the extreme topography of the Tibetan Plateau, this SSTA-induced pattern is more conspicuous in the mid-troposphere and is similar to that associated with the WHD_{PRD}. Under such circumstances, the PRD region is dominated by consistent northerly wind anomalies, facilitating the formation of two key atmospheric processes responsible for a higher WHD_{PRD} (i.e., the transportation of local and nonlocal aerosols and decreased wet deposition tied to the localized suppressed rainfall). An atmospheric general circulation model supported our hypothesis. The anticyclone anomaly tied to the Gill–Matsuno-type response and the remote cyclone anomaly connected to the Gill-type Kelvin wave response were simulated well when we prescribed specified cooling centered over the region to the northwest of NIP.

Funding information This work was financially supported by the National Key R&D Program of China (Grant No. 2018YFC1505803), the Atmospheric Pollution Control of the Prime Minister Fund (Grant No. DQGG0104), the National Natural Science Foundation of China (Grant No. 41605035/41475105), and the National Key Technology Research and Development Program of the Ministry of Science and Technology of China (Grant No. 2014BAC16B06). Zhiwei Zhu is financially supported by the Young Elite Scientists Sponsorship Program by CAST (2018QNRC001).

Compliance with ethical standards

Conflict of interest The authors declare that they have no conflict of interest.

References

Adler RF, Huffman GJ, Chang A, Ferraro R, Xie PP, Janowiak J, Rudolf B, Schneider U, Curtis S, Bolvin D, Gruber A, Susskind J, Arkin P, Nelkin E (2003) The version-2 global precipitation climatology project (GPCP) monthly precipitation analysis (1979–present). J Hydrometeorol 4(6):1147–1167

Chen HP, Wang HJ (2015) Haze days in North China and the associated atmospheric circulations based on daily visibility data from 1960 to 2012. J Geophys Res-Atmos 120(12):5895–5909

Chen MY, Xie PP, Janowiak JE, Arkin PA (2002) Global land precipitation: a 50-yr monthly analysis based on gauge observations. J Hydrometeorol 3(3):249–266

Cheng XG, Zhao TL, Gong SL, Xu XD, Han YX, Yin Y, Tang LL, He HC, He JH (2016) Implications of East Asian summer and winter monsoons for interannual aerosol variations over central-eastern China. Atmos Environ 129:218–228

Cheng X, Boiyo R, Zhao T, Xu X, Gong S, Xie X, Shang K (2019) Climate modulation of Niño3.4 SST-anomalies on air quality change in southern China: application to seasonal forecast of haze pollution. Atmos Res 225:157–164

Dee DP, Uppala SM, Simmons AJ, Berrisford P, Poli P, Kobayashi S, Andrae U, Balmaseda MA, Balsamo G, Bauer P, Bechtold P, Beljaars ACM, van de Berg L, Bidlot J, Bormann N, Delsol C, Dragani R, Fuentes M, Geer AJ, Haimberger L, Healy SB, Hersbach H, Hólm EV, Isaksen L, Kållberg P, Köhler M, Matricardi M, McNally AP, Monge-Sanz BM, Morcrette JJ, Park BK, Peubey C, de Rosnay P, Tavolato C, Thépaut JN, Vitart F (2011) The ERA-Interim reanalysis: configuration and performance of the data assimilation system. Q J R Meteorol Soc 137(656):553–597

Ding YH, Liu YJ (2014) Analysis of long-term variations of fog and haze in China in recent 50 years and their relations with atmospheric humidity. Sci China Earth Sci 57(1):36–46

Feng J, Li J, Liao H, Zhu J (2019) Simulated coordinated impacts of the previous autumn North Atlantic Oscillation (NAO) and winter El Niño on winter aerosol concentrations over eastern China. Atmos Chem Phys 19(16):10787–10800

Gao H, Li X (2015) Influences of El Nino Southern Oscillation events on haze frequency in eastern China during boreal winters. Int J Climatol 35(9):2682–2688

Gill AE (1980) Some simple solutions for heat-induced tropical circulation. Q J R Meteorol Soc 106(449):447–462

He C, Liu R, Wang XM, Liu SC, Zhou TJ, Liao WH (2019) How does El Niño-Southern Oscillation modulate the interannual variability of winter haze days over eastern China? Sci Total Environ 651:1892–1902

Held IM, Suarez MJ (1994) A proposal for the intercomparison of the dynamical cores of atmospheric general circulation models. Bull Am Meteorol Soc 75(10):1825–1830

Huang BY, Thorne PW, Banzon VF, Boyer T, Chepurin G, Lawrimore JH, Menne MJ, Smith TM, Vose RS, Zhang HM (2017) Extended Reconstructed sea surface temperature, version 5 (ERSSTv5): upgrades, validations, and intercomparisons. J Clim 30(20):8179–8205

Jhun JG, Lee EJ (2004) A new East Asian winter monsoon index and associated characteristics of the winter monsoon. J Clim 17(4):711–726

Ji L, Sun S, Arpe K, Bengtsson L (1997) Model study on the interannual variability of Asian winter monsoon and its influence. Adv Atmos Sci 14(1):1–22

Jiang X, Hong C, Zheng Y, Zheng B, Guan D, Gouldson A, Zhang Q, He K (2015) To what extent can China's near-term air pollution control policy protect air quality and human health? A case study of the Pearl River Delta region. Environ Res Lett 10(10):104006

Kalnay E, Kanamitsu M, Kistler R, Collins W, Deaven D, Gandin L, Iredell M, Saha S, White G, Woollen J, Zhu Y, Leetmaa A, Reynolds R, Chelliah M, Ebisuzaki W, Higgins W, Janowiak J, Mo KC, Ropelewski C, Wang J, Jenne R, Joseph D (1996) The NCEP/NCAR 40-year reanalysis project. Bull Am Meteorol Soc 77(3):437–471

Leung DM, Tai APK, Mickley LJ, Moch JM, van Donkelaar A, Shen L, Martin RV (2018) Synoptic meteorological modes of variability for fine particulate matter ($PM_{2.5}$) air quality in major metropolitan regions of China. Atmos Chem Phys 18(9):6733–6748

Li Q, Zhang RH, Wang Y (2016) Interannual variation of the wintertime fog–haze days across central and eastern China and its relation with East Asian winter monsoon. Int J Climatol 36(1):346–354

Li SL, Han Z, Chen HP (2017) A comparison of the effects of interannual Arctic sea ice loss and ENSO on winter haze days: observational analyses and AGCM simulations. J Meteorol Res 31(5):820–833

Li TY, Deng XJ, Li Y, Song YS, Li LY, Tan HB, Wang CL (2018) Transport paths and vertical exchange characteristics of haze pollution in Southern China. Sci Total Environ 625:1074–1087

Luo X, Wang B (2017) How predictable is the winter extremely cold days over temperate East Asia? Clim Dyn 48(7):2557–2568

Mao L, Liu R, Liao W, Wang X, Shao M, Liu SC, Zhang Y (2019) An observation-based perspective of winter haze days in four major polluted regions of China. Natl Sci Rev 6(3):515–523

Matsuno T (1966) Quasi-geostrophic motions in the equatorial area. J Meteorol Soc Jpn 44(1):25–43

Tie XX, Wu D, Brasseur G (2009) Lung cancer mortality and exposure to atmospheric aerosol particles in Guangzhou, China. Atmos Environ 43(14):2375–2377

Tie XX, Huang R-J, Dai WT, Cao JJ, Long X, Su XL, Zhao SY, Wang QY, Li GH (2016) Effect of heavy haze and aerosol pollution on rice and wheat productions in China. Sci Rep 6:29612

Tong CHM, Yim SHL, Rothenberg D, Wang C, Lin C-Y, Chen YD, Lau NC (2018) Projecting the impacts of atmospheric conditions under climate change on air quality over the Pearl River Delta region. Atmos Environ 193:79–87

Wang H, He S (2012) Weakening relationship between East Asian winter monsoon and ENSO after mid-1970s. Chin Sci Bull 57(27):3535–3540

Wang HJ, Chen HP, Liu JP (2015) Arctic sea ice decline intensified haze pollution in eastern China. Atmos Ocean Sci Lett 8(1):1–9

Wang J, Zhang M, Bai X, Tan H, Li S, Liu J, Zhang R, Wolters MA, Qin X, Zhang M, Lin H, Li Y, Li J, Chen L (2017) Large-scale transport of $PM_{2.5}$ in the lower troposphere during winter cold surges in China. Sci Rep 7(1):13238

Wang J, Zhao QH, Zhu ZW, Qi L, Wang JXL, He JH (2018) Interannual variation in the number and severity of autumnal haze days in the Beijing–Tianjin–Hebei region and associated atmospheric circulation anomalies. Dyn Atmos Oceans 84:1–9

Wang J, Zhu ZW, Qi L, Zhao QH, He JH, Wang JXL (2019) Two pathways of how remote SST anomalies drive the interannual variability of autumnal haze days in the Beijing–Tianjin–Hebei region, China. Atmos Chem Phys 19(3):1521–1535

Wu D, Tie XX, Li CC, Ying ZM, Kai-Hon Lau A, Huang J, Deng XJ, Bi XY (2005) An extremely low visibility event over the Guangzhou region: a case study. Atmos Environ 39(35):6568–6577

Wu D, Bi XY, Deng XJ, Li F, Tan H, Liao GL, Huang J (2007) Effect of atmospheric haze on the deterioration of visibility over the Pearl River Delta. Acta Meteorologica Sinica 21(2):215–223

Wu M, Wu D, Fan Q, Wang BM, Li HW, Fan SJ (2013) Observational studies of the meteorological characteristics associated with poor air quality over the Pearl River Delta in China. Atmos Chem Phys 13(21):10755–10766

Wu Z, Zhang Y, Zhang L, Huang M, Zhong L, Chen D, Wang X (2019) Trends of outdoor air pollution and the impact on premature mortality in the Pearl River Delta region of southern China during 2006–2015. Sci Total Environ 690:248–260

Xiao D, Li Y, Fan SJ, Zhang RH, Sun JR, Wang Y (2015) Plausible influence of Atlantic Ocean SST anomalies on winter haze in China. Theor Appl Climatol 122(1):249–257

Yang Y, Liao H, Lou SJ (2016) Increase in winter haze over eastern China in recent decades: roles of variations in meteorological parameters and anthropogenic emissions. J Geophys Res Atmos 121(21):13,050–13,065

Yin Z, Wang H, Ma X (2019) Possible relationship between the Chukchi Sea ice in the early winter and the February haze pollution in the North China Plain. J Clim 32(16):5179–5190

You YC, Cheng XG, Zhao TL, Xu XD, Gong SL, Zhang XY, Zheng Y, Che HZ, Yu C, Chang JC, Ma GX, Wu M (2018) Variations of haze pollution in China modulated by thermal forcing of the Western Pacific Warm Pool. Atmosphere 9(8):314

Yu JH, Li T, Tan ZM, Zhu ZW (2016) Effects of tropical North Atlantic SST on tropical cyclone genesis in the western North Pacific. Clim Dyn 46(3):865–877

Zhang X, Xu X, Ding Y, Liu Y, Zhang H, Wang Y, Zhong J (2019) The impact of meteorological changes from 2013 to 2017 on $PM_{2.5}$ mass reduction in key regions in China. Sci China Earth Sci 62(12):1885–1902

Zhao SY, Zhang H, Xie B (2018) The effects of El Niño–Southern Oscillation on the winter haze pollution of China. Atmos Chem Phys 18(3):1863–1877

Zheng Y, Xue T, Zhang Q, Geng G, Tong D, Li X, He K (2017) Air quality improvements and health benefits from China's clean air action since 2013. Environ Res Lett 12(11):114020

Zhu ZW, Li T (2016) A new paradigm for continental U.S. summer rainfall variability: Asia–North America teleconnection. J Clim 29(20):7313–7327

Zhu ZW, Li T (2017) The record-breaking hot summer in 2015 over Hawaii and its physical causes. J Clim 30(11):4253–4266

Zhu ZW, Li T (2018) Amplified contiguous United States summer rainfall variability induced by East Asian monsoon interdecadal change. Clim Dyn 50(9):3523–3536

Zou YF, Wang YH, Zhang YZ, Koo J-H (2017) Arctic sea ice, Eurasia snow, and extreme winter haze in China. Sci Adv 3(3):e1602751